Al$_2$O$_3$ microring resonators for the detection of a cancer biomarker in undiluted urine

M. DE GOEDE,[1] M. DIJKSTRA,[1] R. OBREGÓN,[2] J. RAMÓN-AZCÓN,[2] E. MARTÍNEZ,[2,3,4] L. PADILLA,[5] F. MITJANS,[5] AND S. M. GARCIA-BLANCO[1,*]

[1]Optical Sciences Group, MESA + Institute for Nanotechnology, University of Twente, P.O. Box 217, 7500 AE Enschede, The Netherlands
[2]Institutue for Bioengineering of Catalonia (IBEC), The Barcelona Institute of Science and Technology (BIST), Baldiri Reixac 10-12, 08028 Barcelona, Spain
[3]Department of Electronics and Biomedical Engineering, University of Barcelona (UB), Barcelona 08028, Spain
[4]Centro de Investigación Biomédica en Red (CIBER), Madrid 28029, Spain
[5]Health & Biomedicine unit of LEITAT Technological Center, Barcelona Science Park, Barcelona 08028, Spain
*s.m.garciablanco@utwente.nl

Abstract: Concentrations down to 3 nM of the rhS100A4 protein, associated with human tumor development, have been detected in undiluted urine using an integrated sensor based on microring resonators in the emerging Al$_2$O$_3$ photonic platform. The fabricated microrings were designed for operation in the C-band (λ = 1565 nm) and exhibited a high-quality factor in air of 3.2×10^5. The bulk refractive index sensitivity of the devices was ~100 nm/RIU (for TM polarization) with a limit of detection of ~10^{-6} RIU. A surface functionalization protocol was developed to allow for the selective binding of the monoclonal antibodies designed to capture the target biomarker to the surface of the Al$_2$O$_3$ microrings. The detection of rhS100A4 proteins at clinically relevant concentrations in urine is a big milestone towards the use of biosensors for the screening and early diagnosis of different cancers. Biosensors based on this microring technology can lead to portable, multiplexed and easy-to-use point of care devices.

1. Introduction

Early diagnostic of diseases will permit treatment before symptoms emerge, greatly increasing the survival rate and the quality of life of patients. In particular, screening for different types of cancer will help reducing the impact of this disease, which is one of the main causes of death in developed countries [1]. The monitoring of the pre- and post-operative evolution of cancer patients is also of major significance. The S100 proteins family is associated with a regulatory role in a variety of cellular processes [2]. Many lines of investigation suggest that overexpression of S100 proteins is associated with tumor progression and prognosis [3,4]. S100A4 is a member of this family and it is found as a highly expressed transcript in metastatic tumor cell lines. S100A4 is up-regulated in several malignancies including bladder cancer and plays a role in tumor aggressiveness [5–7]. Therefore, the overexpression of S100A4 protein may be of value as a biomarker of bladder cancer progression. Urine levels of S100A4 for bladder cancer are not reported in the literature but Turnier et al. showed median urine levels of S100A4 around 0.1 nM for healthy controls and median urine levels ranging from 0.5 to 1 nM for patients with lupus nephritis using a commercially available ELISA kit [8].

At present, there are several commercial assays for bladder cancer diagnosis based on immunoassays, but they have high variability of sensitivity and specificity. In addition, in

most of them the false-positive rate is quite high, they require tedious/laborious assay procedures, are time consuming, expensive and need specialized personnel [9,10]. To this aim, the development of portable, low cost, multiplexed and easy to use devices that, within minutes, can detect cancer biomarkers directly from biofluids is instrumental.

Integrated optical sensors are good candidates for the label-free detection of molecular biomarkers [11–13]. Microring resonator (MRR) based biosensors have shown high sensitivity and limit of detection compatible with clinical relevant needs [14,15]. Their operation is based on the wavelength shift of the narrow dips in their transmission spectrum induced by variations of the refractive index probed by the evanescent field. When their surfaces are functionalized with capture probes and biomarkers are bound to them, such binding induces refractive index changes that result in detectable wavelength shifts that can be used for biosensing. Limits of detection (LOD) around 10^{-6} RIU (refractive index units) are typically achieved using integrated MRR sensors [16,17]. The LOD is limited by the noise of the system due to temperature fluctuations and laser wavelength or intensity variations [18]. Label-free detection of biomarkers using MRRs has been demonstrated in different integrated photonic platforms, including silicon-on-insulator (SOI) [19–21], silicon oxynitride [22] and silicon nitride [23]. However, biological samples, such as blood, urine or saliva, are complex matrices that must be properly processed to remove interfering substances (proteins, metabolites). That pre-treatment is a tedious and critical step and it is not conducive to on-line processing and automation. In addition, the concentration of the biomarkers in clinical samples is often at nanomolar level or lower, and most of these references use amplification strategies to achieve clinically relevant LOD, which add a complexity to the system, associated to non-label free strategies [24–26].

Label-free detection of cancer biomarkers from buffer samples containing fetal bovine serum at a detection limit of 25 ng/ml was reported by Washburn et. al. with MRRs based on SOI technology [27]. More recently, Shin. et. al. realized label-free detection of bladder cancer DNA biomarkers from urine, although at quite high concentrations in the μM range, which are not useful for monitoring or early diagnostics [28]. To use MRR as sensitive and selective biosensors for clinical samples with good LOD, requires efficient functionalization strategies that allow anchoring the capture probes on the surface to selectively recognize the biomarker of interest.

Aluminum oxide (Al_2O_3) is an emerging photonic material that, unlike the silicon-based technologies, has not been explored yet for biosensing applications. It has attractive features such as a low waveguide propagation loss down to 0.21 ± 0.05 dB/cm at a wavelength of 1550 nm [29] and a large transparency window ranging from the visible to the mid-infrared [30], exceeding that of SOI and making this material very interesting for the realization of optical sensors working in the visible, near and mid-infrared wavelength ranges. Furthermore, this material has the possibility of being doped with rare earth ions to achieve optical gain and active functionalities [31–34]. This feature allows for the development of laser-based biosensors to achieve narrower linewidths, higher sensitivities and novel sensing functionalities [35,36]. However, the only reports of optical sensors using the Al_2O_3 photonic platform are the realization of a dual-wavelength Al_2O_3 distributed feedback laser whose evanescent field was used to detect the presence of glass microspheres of diameters ranging between 1 μm and 20 μm [37] and the usage of an Al_2O_3:Yb^{3+} microdisk laser integrated on chip and operating in an aqueous environment to detect minute bulk refractive index variations [38]. Furthermore, high quality factor (Q) undoped Al_2O_3 MRRs were recently demonstrated by Su et al. [39], although they were not utilized for biosensing applications. The work presented here serves as a validation of using the undoped Al_2O_3 material platform for optical biosensors, with the prospects of expanding this platform by including dopants for active sensing functionalities.

In this work, we demonstrate the development of MRR biosensors based on the Al_2O_3 photonic platform with high sensitivity and low limit of detection. First, the MRR devices

were fully characterized, including their bulk refractive index and temperature sensitivity [40]. Performance on par with the silicon-based technologies is demonstrated. Then, the devices were tested for the detection of the rhS100A4 protein biomarker in undiluted urine. A limit of detection of 3 nM (~36 ng/ml) was demonstrated. This value lies within the clinically relevant range demonstrated by Turnier et al. for patients with lupus nephritis and can be used as a reference value for patients with bladder cancer [8,41,42]. These results show the potential of using this novel material platform to detect biomarkers in point-of-care applications using patients' urine without any sample pre-treatment and/or complicated amplification steps.

2. Sensor platform design and fabrication

Waveguide MRRs were developed as biosensors on the Al_2O_3 material platform. Their wavelength dependent transmission spectra contain multiple resonance wavelengths whenever light inside the MRR has a roundtrip phase multiple of 2π (i.e., the resonance condition). Upon a variation of the refractive index of the environment of the MRR, the total roundtrip phase changes and the resonance wavelength shifts. By monitoring this shift, the MRR can be used as a refractive index sensor with a sensitivity S given by [43]:

$$S = \frac{\lambda}{n_g} \frac{\partial n_{\text{eff}}}{\partial n}$$ (1)

where λ is the resonance wavelength of the MRR, n_g is the group index of the waveguide, n_{eff} is the effective refractive index of the waveguide and n is the refractive index of the medium surrounding the waveguide. To ensure a high sensitivity, the derivative in Eq. (1) should be as high as possible, which can be realized by a waveguide design that has a large evanescent tail in the top cladding or, alternatively, by engineering the waveguide dispersion to reduce the group index [44].

Associated with the bulk refractive index sensitivity is the limit of detection (LOD). It characterizes the smallest variation of bulk refractive index that can still be reliably measured by the MRR and it is given by [18]:

$$\text{LOD} = \frac{3\varepsilon}{S}$$ (2)

where ε is the uncertainty or signal noise in the determination of the resonance wavelength. The uncertainty scales with the width of the resonance, i.e., its Q. Optimal sensing performance requires a low LOD, and thus a high S and low ε. However, extending the evanescent tail to increase the sensitivity can result in decreased Q due to increased bend radiation loss and absorption losses in the sensing medium, constraining the MRR waveguide design.

The Al_2O_3 MRRs were designed to operate for both TE and TM polarization in the telecom band (λ = 1565 nm) to demonstrate compatibility with the widely available instrumentation used by the SOI platform. Furthermore, the waveguide should support only a single mode for both polarizations to avoid higher-order resonances in the transmission spectrum that would complicate the analysis and resonance wavelength monitoring. Finally, the MRRs are designed to be critically coupled and to exhibit high Q to ensure deep, sharp dips that will ease their curve fitting and reduce the noise in the extraction of the sensor parameters.
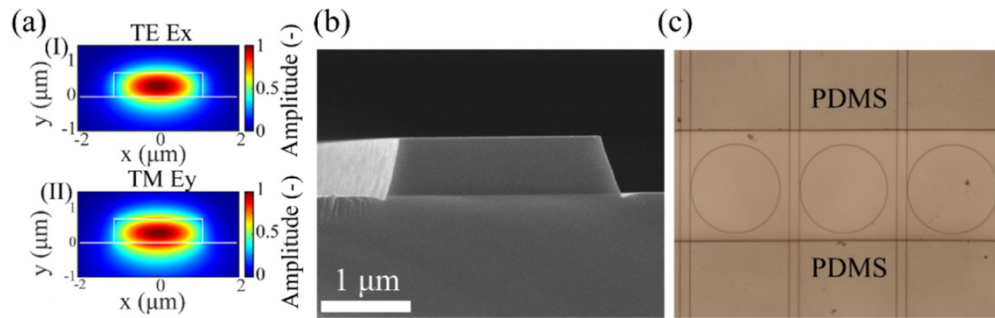
Fig. 1. (a) Mode profile of the fundamental mode for respectively TE polarization (I) and TM polarization (II). (b) Scanning electron microscope image of the Al_2O_3 waveguide cross section. (c) Optical microscope image of the MRRs inside the PDMS microfluidic flow channel.

The MRR was modelled using a combination of an analytical MRR model with a numerical waveguide solver [45] to determine its geometric parameters. Fully vectorial 2D eigenmode calculations (Lumerical MODE solutions) were performed to determine the bend radiation loss, the power coupling from the bus waveguide to the MRR, and the S at a central wavelength of 1565 nm. At this wavelength, the bottom SiO_2 cladding, the Al_2O_3 waveguide core material and the water top cladding have refractive indices of 1.46, 1.65 and 1.33 RIU, respectively. The optimum parameters for the MRR were determined to be a waveguide cross section of 2.0×0.7 μm^2 for both the bus and MRR waveguide, a coupling gap of 0.8 μm, and a MRR radius of 200 μm. Figures 1(a) and 1(b) show the designed waveguide cross section with the dominant component of the modal field for respectively TE and TM polarization.

These design parameters were used for the MRR fabrication. First, a 700-nm-thick Al_2O_3 layer was deposited by reactive sputter deposition on an oxidized silicon substrate (i.e., thickness of thermal oxide of 8 μm) with an AJA ATC 1500 sputter coater. Then, the bus waveguides and MRRs were patterned with contact UV lithography and subsequently etched with an Oxford Plasmalab System 100 inductively coupled plasma reactive ion etcher with a plasma of BCl_3 and HBr at a ratio of 5:2. Figure 1(b) displays the resulting waveguide cross section. A SiO_2 top cladding was then locally deposited with PECVD using a shadow mask to cover the bus waveguide while leaving the MRRs exposed to address them with an aqueous environment. Finally, a PDMS microfluidic device with a 600 μm wide and 70 μm high channel, shown in Fig. 1(c), was bonded onto diced, cleaned and chemically activated chips containing the MRRs.

3. Experimental

3.1. MRR characterization set up

To optically characterize the Al_2O_3 MRRs, an optofluidic experimental set up was developed and is shown in Fig. 2(a). The MRR chip was placed on the sample holder by vacuum connection. A Peltier driven temperature controller was used to drive the temperature of the sample holder within $\sim \pm 0.01°C$. Laser light from an Agilent 81646 tunable laser was guided through single mode polarization maintaining fibers (PM1550-XP, mode field diameter of 10.1 μm) and butt coupled to the chip's end facets using index-matching fluid. For alignment of the fibers to the chip, a piezo-controlled micropositioner was used. To perform the alignment procedure, a red Helium-Neon (HeNe) laser was coupled into the device, as can be seen in Fig. 2(b). Finally, a syringe pump was connected to the PDMS microfluidic chip and used to flow liquid samples over the MRRs.
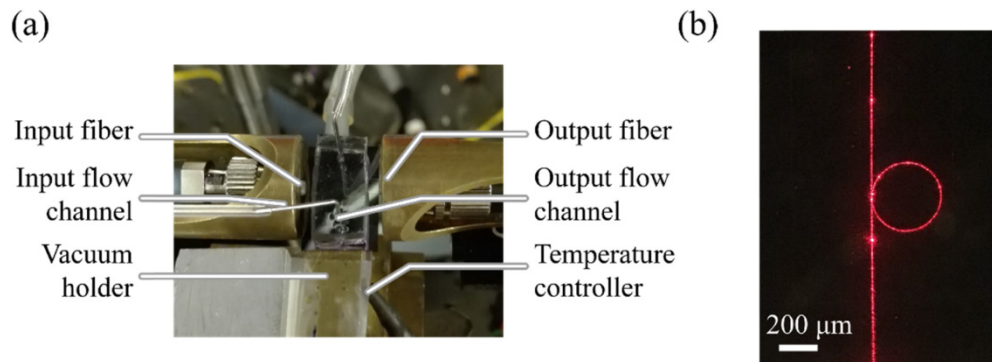
Fig. 2. (a) Photograph of the optofluidic chip mounted on the experimental setup. The chip has dimensions of 1.2×1.9 cm^2. (b) Optical microscope image of the MRR and bus waveguide upon coupling red light from a HeNe laser into the device.

Wavelength dependent transmission spectra of the MRRs were measured. For all following experiments, this was done at a rate of ~7 spectra per minute. The polarization was controlled by the fiber alignment. The transmission spectra were obtained for TE and TM polarized light for either a top cladding of air or while being submerged in H$_2$O. The wavelength range was between $\lambda = 1545$ and 1570 nm with a resolution of 1 pm. To extract the propagation loss and resonance quality factor Q, the resonance peaks were fitted with a Lorentzian function to extract the MRR loss and coupling coefficients [46]. For the sensing experiments, the location of the resonance wavelength was extracted from repeatedly acquired transmission spectra over time for enhanced precision and reduced noise.

The sensing performance of the MRR is characterized by measuring its bulk refractive index sensitivity and temperature sensitivity for both TE and TM polarized light. To determine the bulk refractive index sensitivity, deionized water and NaCl solutions were flown over the device. By increasing the concentration of NaCl, the refractive index of the deionized water can be varied by 0.0018 RIU/wt% [47]. Solutions with NaCl concentrations ranging from 0.05 wt% to 0.30 wt% were prepared and flown over the MRRs at a rate of 100 µl/min, while simultaneously recording the transmission spectra to monitor the shift of the resonance wavelength. The stage temperature was kept fixed at 21.5°C. To determine the temperature sensitivity, the resonance wavelength shift was measured upon varying the temperature of the stage while immersing the MRR in deionized water at a flow rate of 10 µl/min. The temperature was increased in steps of ~0.5°C every 4 minutes.

3.2. Biosensing protocol

Recombinant human S100A4 (rhS100A4) protein was obtained as described by [48]. Hybridoma obtaining and cell subcloning was performed using standard technologies. Briefly, mice were immunized with hrS100A4 and B cells were fused with myeloma cells to obtain hybridoma cells. After cell subcloning, serum free supernatant of the selected antibody-secreting hybridoma cell line was obtained and purified using protein A columns (MabSelect SureTM LX; Amersham) and an ÄKTA purifier FPLC system (GE Healthcare).

For the sensitive and selective detection of biomolecules, a robust protocol for the covalent binding of the capture antibodies (Ab) to the Al$_2$O$_3$ surface was developed in our laboratory. Briefly, the Al$_2$O$_3$ surface was activated with O$_2$ plasma and a carboxylic acid-terminated layer was deposited. After the activation of the carboxylic terminals by an EDC/NHS reaction the MRR chips are ready for anchoring the capture antibody on its surface. The surface functionalization process developed permitted the preferential binding of antibodies to the Al$_2$O$_3$ material. Molecular recognition reactions would then guarantee that rhS100A4 proteins contained in the sample would bind to the surface immobilized antibodies

selectively. Figure 3(a) shows a schematic outline of the procedure used to functionalize the surface of the MRR. First, the MRR chip was cleaned with deionized water, acetone and ethanol to remove organic surface contaminants. Afterwards, to activate the surface for functionalization, the chip was cleaned with HNO_3 and O_2 plasma. After O_2 plasma activation, the surface was modified with 6-phosphonohexanoic acid (500 µM, anhydrous heptane) and, after solvent evaporation, it was heated in an oven at 120°C for 12 hours to form a carboxylic acid-terminated layer. For Ab immobilization, the chip was immersed in a carboxylic acid activating solution (1-Ethyl-3-(3 dimethylaminopropyl)carbodiimide (EDC) 25 mM, N-Hydroxysuccinimide (NHS) 50 mM, in 100 mM MES buffer, pH 4.7) for 2 hours, and gently washed with deionized water. To test the successful immobilization of antibodies on the surface, a fluorescence assay was carried out with an antibody labelled with fluorescein isothiocyanate fluorescence dye (10 µg/ml), as shown in Fig. 3(b).

The PDMS microfluidic channel was bonded to the chemically functionalized MRRs and the flow rate was set at 100 µl/min. First, a solution containing Anti-S100A4 antibody at 50 µg/ml in phosphate buffered saline (PBS) 10 mM was delivered until the reading signal was saturated, therefore indicating that a layer of capture probes was formed on the chemically functionalized surfaces. Then, a solution of bovine serum albumin (BSA) 1% in PBS 10 mM was flown to prevent nonspecific biomolecule adsorption.

A urine sample was pooled from six healthy women. A 10 v/v% of PBS 100 mM was added to this urine, and the pH was adjusted to 7.5 by adding NaOH. Pooled urine samples were filtered with a 0.2 µm pore filter and stored at 4°C before use. Then, different amounts of the rhS100A4 protein were added to the urine samples to obtain samples spiked with known biomarker concentrations ranging from 3000 nM down to 3 nM. These samples were then flown over the biosensor at 100 µl/min for 10 min and the sensor response was monitored on-line. During the biosensing experiments the stage temperature was kept fixed at 21.5°C.
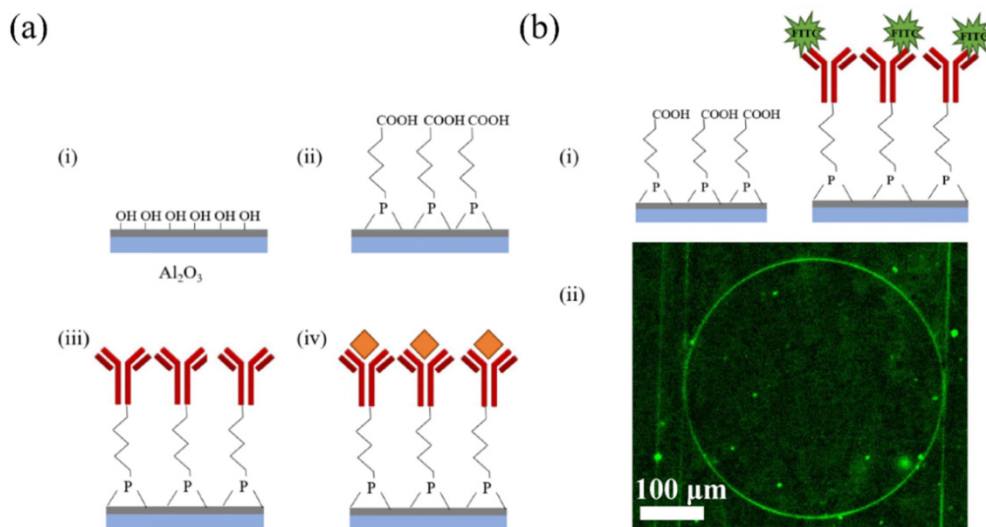

Fig. 3. (a) Schematic representation showing the developed Al_2O_3 surface functionalization protocol. (i) Surface activation with O_2 plasma. (ii) 6-phosphonohexanoic acid, 500 µM in anhydrous heptane, reacts with the Al_2O_3 surface to generate a carboxylic acid-terminated surface. (iii) Activation of carboxylic terminals by EDC/NHS and anti-S100A4 antibody immobilization. (iv) Protein recognition. (b) (i) Schematic representation of the fluorescence assay to verify the immobilization of antibody capture probes. (ii) Microscope fluorescent image of Al_2O_3 ring functionalized with 6-phosphonohexanoic acid and immobilized with an antibody labelled with fluorescein isothiocyanate fluorescence dye (FITC, 495 nm/519 nm excitation/emission). Magnification 40x, acquisition time 2000 ms.

4. Results and discussion

4.1. MRR characterization

Wavelength-dependent transmission spectra of the Al_2O_3 MRRs were obtained for the TE and TM polarizations for both claddings of air and deionized water. Figures 4(a) and 4(b) show the sharp, deep resonance peaks present in the transmission spectra. The data was normalized by subtracting the background fitted by a high-order polynomial, followed by fitting the resonance peaks with a Lorentzian function. From the fit, the extinction ratio and full width half maximum were obtained, which were used to retrieve the waveguide propagation loss and loaded quality factors.

A high quality factor and low optical loss inside the MRR are necessary for optimal sensing performance. Various repetitions of the design parameters were fabricated on the chips and measured. Out of them, the MRR design with the best performance was selected for the sensitivity and biosensing experiments. For this optimal MRR a loaded quality factor of $Q = 3.2 \pm 0.2 \times 10^5$ was found for TE polarization with an air cladding, corresponding with an optical propagation loss of 0.60 ± 0.04 dB/cm. For TM polarization with an air cladding, a Q of $9.6 \pm 0.5 \times 10^4$ together with an optical loss of 2.00 ± 0.19 dB/cm were measured. The increased loss is due to the lesser confinement of the mode for TM polarization, exhibiting therefore higher bend and sidewall radiation loss. Since the devices were nearly critically coupled, these results would correspond with a highest intrinsic quality factor $Q_i \sim 6 \times 10^5$, a value similar as found by Su et al. [39]. However, an advantage of the Al_2O_3 MRRs presented here is that the fabrication process is simpler and requires only a single deposition and etching step. Furthermore, in principle the Q could be further increased by making the MRR waveguide both wider and thicker, to reduce the bend radiation loss and decrease the modal overlap with the sidewall roughness. However, this would come at the expense of reduced sensitivity and multimodal operation.
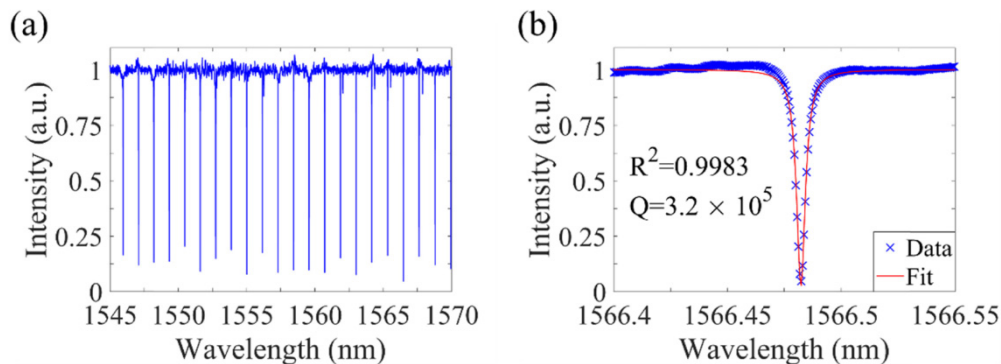

Fig. 4. (a) MRR transmission spectrum for TE polarized light and a top cladding of air. (b) Lorentzian fit of one of the resonances in (a).

The Q and optical loss analysis of the MRRs was repeated for a cladding of deionized water. Then, the Q dropped for both the TE and TM polarization, due to the optical absorption of the water in this wavelength range. The Qs were determined at 5.6×10^4 and 4.4×10^4 for TE and TM polarization respectively, corresponding with optical propagation losses of 4.0 ± 0.6 and 5.7 ± 0.7 dB/cm, respectively. These results are summarized in Table 1.

Table 1. Summary of Al$_2$O$_3$ MRR optical loss.

Polarization	Air		Deionized water	
	Q (-)	α (dB/cm)	Q (-)	α (dB/cm)
TE	$3.2 \pm 0.2 \times 10^5$	0.60 ± 0.04	$5.9 \pm 8.0 \times 10^4$	4.0 ± 0.6
TM	$9.6 \pm 0.5 \times 10^4$	2.00 ± 0.19	$4.5 \pm 5.0 \times 10^4$	5.7 ± 0.7

4.2. Bulk refractive index and temperature sensitivity

The bulk refractive index sensitivity and LOD of the MRR with highest Q were characterized by flowing deionized water and NaCl solutions over the device while repeatedly recording the transmission spectra. Figure 5(a) shows the shift of the resonance peak for various NaCl concentrations. Due to the higher refractive index of the top cladding, the n_{eff} increases, resulting in a positive shift of the resonance wavelength. The real-time response was recorded by monitoring the resonance wavelength shift over time while flowing different liquids and can be seen in Fig. 5(b). The drops of the resonance wavelength shifting down to the water baseline signal correspond to switching between the different NaCl solutions. Figure 5(c) shows the determined bulk refractive index sensitivities, which amount to 70.8 ± 0.6 nm/RIU and 102.3 ± 0.5 nm/RIU for TE and TM polarizations, respectively. Due to the modal field being less confined for the TM polarization, its bulk refractive index sensitivity is higher than that for TE polarization.
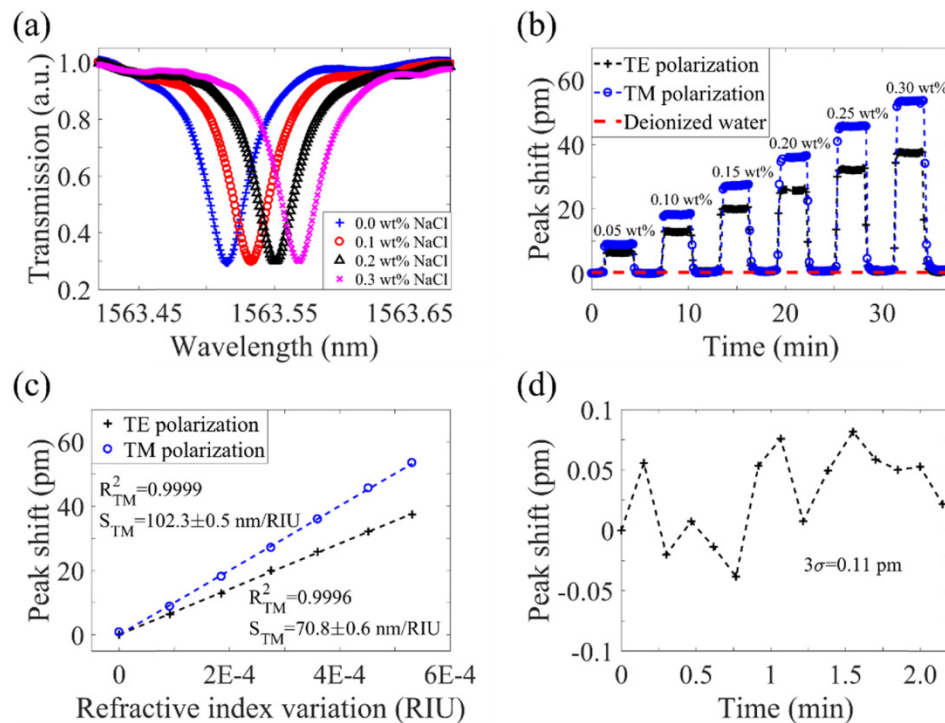

Fig. 5. (a) Shift of resonance wavelength peak for bulk refractive index variation of the water flow over the MRR for TM polarization. (b) Real-time monitoring of the shift of the resonance wavelength during bulk refractive index sensing for both TE and TM polarization. The flow was switched every 3 minutes between deionized water and NaCl solutions with concentrations ranging from 0.30 wt% down to 0.05 wt%. The flow rate was 100 µl/min. (c) Resonance wavelength shift for variations of the bulk refractive index. (d) Resonance wavelength noise during the bulk refractive index experiment for TM polarization.

The MRR is subjected to wavelength and intensity noise, which impose an uncertainty on the determination of the resonance wavelength. This can be lowered by repeatedly acquiring spectra and fitting their resonance wavelengths, followed by averaging the results [49]. For the bulk refractive index sensing the uncertainty is the standard deviation of the fitted resonance wavelength during a time interval of 2 minutes, or 15 repeated measurements and is shown in Fig. 5(d). This time corresponds with the duration of the MRR exposure time to the liquid to be sensed. The standard deviation in the resonance wavelength was determined and yielded a noise of $3\sigma = 0.11$ pm for TM polarization. Combining the measured bulk refractive index sensitivities with the measured detection noise yields a highest LOD of 1.1×10^{-6} RIU for TM polarization, a value similar to the best reported results achieved with SOI and silicon nitride MRR refractive index sensors [16,23].

The MRR's temperature sensitivity was determined by monitoring the shift of the resonance wavelength over time while increasing the stage temperature, as shown in Figs. 6(a) and 6(b). Temperature sensitivities of 8.1 ± 0.1 pm/K and 4.3 ± 0.1 pm/K were measured for TE and TM polarizations, respectively. The latter is lower since more modal power resides in the aqueous top cladding that has a negative thermo-optic coefficient [47]. A lower temperature sensitivity is desirable for a lower resonance wavelength noise and drift. The measured higher bulk refractive index sensitivity combined with the lower temperature sensitivity motivated to operate the MRR in TM polarization for the biosensing experiments.
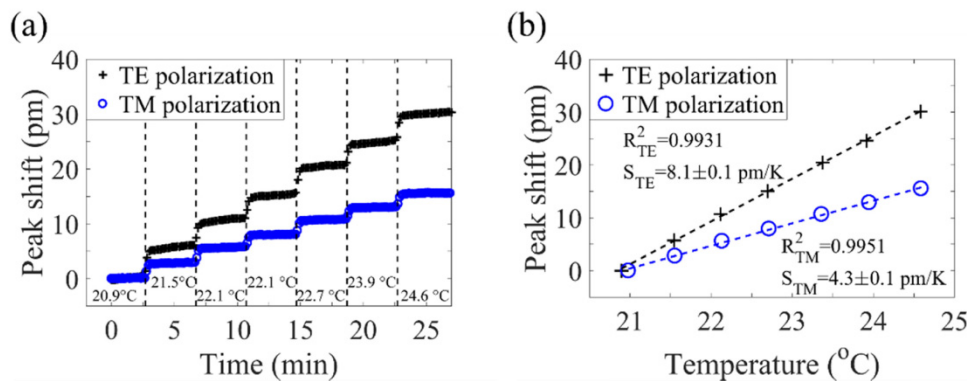

Fig. 6. (a) Real-time monitoring of the shift of the resonance wavelength while varying the stage temperature for both TE and TM polarized light. Deionized water was flown over the MRR at a rate of 100 μl/min. (b) Resonance wavelength shift as function of the stage temperature.

4.3. Cancer biomarker detection in urine

Figure 7(a) shows all the steps of the biosensing experiment and the real-time monitoring of antibody immobilization and protein recognition events. The first phase consists of a washing step with PBS until a stable baseline was obtained. The second phase is the coating of the MRR surface with the anti-S100A4 monoclonal Ab at 50 μg/ml in PBS. After 20 min, a stable baseline was observed, indicating that no more binding events occur and that the MRR surface is saturated with Ab capture probes. The subsequent washing step with PBS removes all the non-covalently bound Ab. The lack of a considerable resonance wavelength shift here indicates that the Ab is strongly bound to the MRR surface. The third phase consists of a blocking step with BSA to prevent nonspecific adsorption. The washing step showed just a small net shift, confirming that most of the biosensor surface was covered during the Ab immobilization. Then, the biosensor was exposed to a sample of pooled urine without rhS100A4 protein. A large resonance wavelength shift due to the difference in bulk refractive index between urine and PBS was observed. Finally, the fifth phase introduces the urine containing the protein biomarkers.

The biosensing assay was carried out with urine samples containing known concentrations of rhS100A4 ranging from 3000 nM down to 3 nM. Figure 7(b) shows the response of the biosensor to different concentrations of the protein. For visibility, the two highest concentrations tested were omitted (400 and 3000 nM). After 8 minutes, the total wavelength shift was recorded and plotted as function of biomarker concentration in Fig. 7(c). As a general trend for all concentrations, it can be observed that the resonance wavelength shifts to higher values due to protein binding to the Ab, with higher concentrations corresponding with larger total shifts. Furthermore, for the highest concentrations the total shift saturates, indicating that equilibrium between binding and disassociation of the proteins to the Ab has been achieved.

For the biosensing experiment in urine, the uncertainty is defined as the total resonance wavelength drift during the 8 minutes measurement interval of a blank urine sample, as shown in Fig. 7(d). In this case, a drift of ~0.05 pm/min was measured, which is most likely due to some non-specific binding or buildup of material on the MRR. In this case, the LOD is the smallest protein concentration that yields a total shift that is equal to or larger than three times this drift (i.e., 1.2 pm). At an rhS100A4 protein concentration of 3 nM, a total resonance wavelength shift of 1.43 pm was measured after 8 minutes of measurement, establishing the limit of detection of this system at 3 nM, which lies within the clinically range demonstrated by Turnier et al.

Figure 7(e) shows the selectivity test of the biosensing procedure by performing two control experiments. First, 400 nM rhS100A4 protein was flown over a MRR without Ab immobilized on its surface. The resulting resonance wavelength shift (6.3 pm) is ~10 times smaller than that of a MRR with Ab immobilized for the same protein concentration (59.9 pm). Second, a urine sample containing neutravidin protein, which should not be bound to the Ab upon molecular recognition, was flown over the biosensor. Indeed, the resulting resonance wavelength shift for the sample containing neutravidin was 20 times smaller (3.1 pm) than that for the rhS100A4 protein. These results indicate that our biosensing platform using anti-S100A4 antibodies is highly selectively in sensing hrS100A4 proteins.

The platform described herein, is sensitive and selective for hrS100A4 protein detection in undiluted urine. By immobilizing other selective probes onto the surface, it is possible to confer target-specific binding properties and thus develop a multiplexed system to detect several biomarkers with a small volume of sample and within a few minutes. Future work will focus on developing a multiplexed platform to obtain multiple clinically relevant measurements from a single sample.
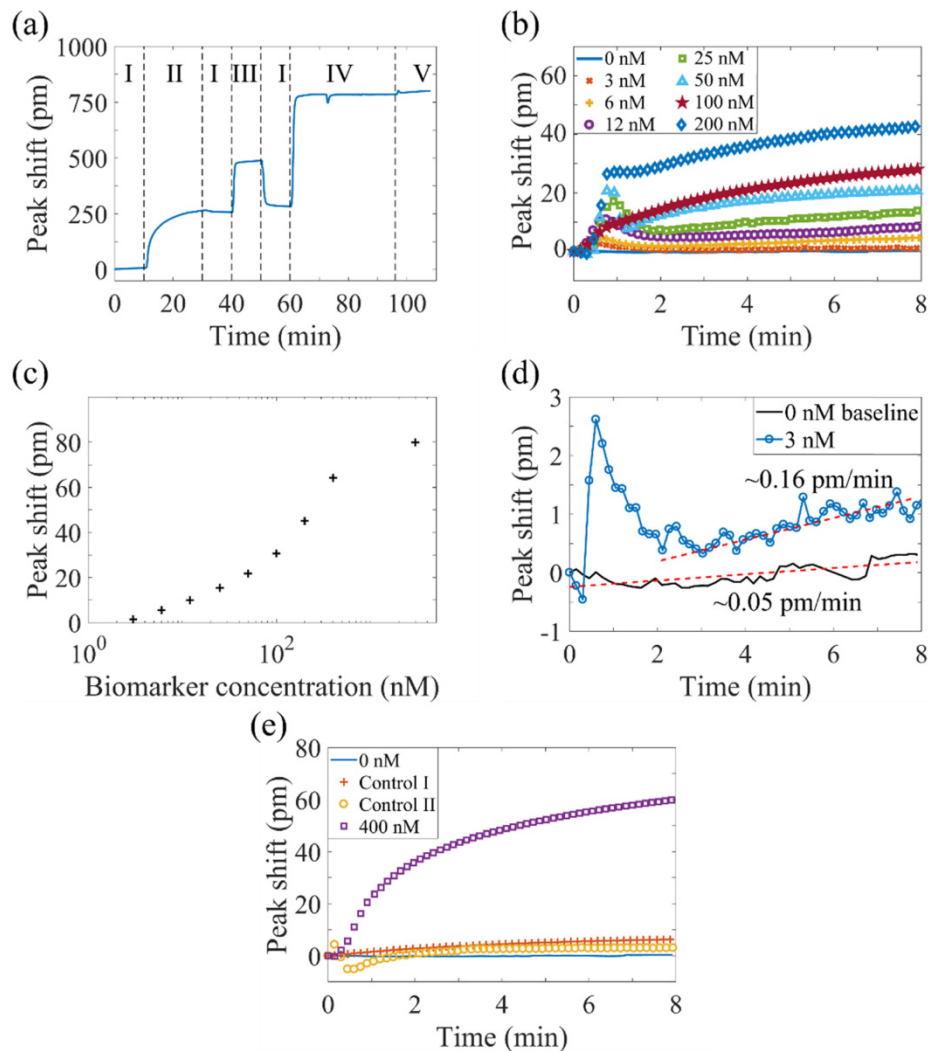
Fig. 7. (a) MRR sensorgram. The MRR was addressed with PBS 10 mM (I), anti-S100A4 antibody at 50 µg/ml (II), BSA 1% in PBS (III), urine (IV), and rhS100A4 at 25 nM in urine (V). The flow rate was 100 µl/min. (b) Binding of rhS100A4 to the antibodies immobilized onto the MRR's surface. The initial bumps results from the dynamics of the flow system. (c) Resonance wavelength shift as function of rhS100A4 concentration. (d) Resonance wavelength noise for a blank urine sample. (e) Selectivity assay for anti-S100A4 antibody in urine. Control I: rhS100A4 at 400 nM, without antibody coated on the surface. Control II: neutravidin at 400 nM in urine.

5. Conclusion

To conclude, the Al_2O_3 photonic platform developed here appears as a very promising biosensor platform. Its bulk refractive index sensitivity of ~100 nm/RIU and LOD of ~10^{-6} RIU are comparable with the more mature SOI and silicon nitride technologies. A robust surface functionalization protocol was developed that permits a good coverage of the surface of the Al_2O_3 sensor with antibodies. The label-free detection of 3 nM of the rhS100A4 protein, associated with cancer disease, was demonstrated in whole urine without the need of neither sample pre-treatment nor signal amplification steps and within less than ten minutes. Also, MRR offer real-time monitoring capacity in contrast with commercial immunoassay kits that only offer endpoint readout. The particular attributes of rapid response, small volume

of sample, simple format and easy to use, lend Al_2O_3 biosensing platform to be used as a point-of-care device with real patient samples in clinical environments.

Funding

Acknowledgments

References

1. F. Bray, J. Ferlay, I. Soerjomataram, R. L. Siegel, L. A. Torre, and A. Jemal, "Global cancer statistics 2018: GLOBOCAN estimates of incidence and mortality worldwide for 36 cancers in 185 countries," CA Cancer J. Clin. **68**(6), 394–424 (2018).
2. A. R. Bresnick, D. J. Weber, and D. B. Zimmer, "S100 proteins in cancer," Nat. Rev. Cancer **15**(2), 96–109 (2015).
3. H. Chen, C. Xu, Q. Jin, and Z. Liu, "S100 protein family in human cancer," Am. J. Cancer Res. **4**(2), 89–115 (2014).
4. N. Bansal, A. K. Gupta, A. Gupta, S. N. Sankhwar, and A. A. Mahdi, "Serum-based protein biomarkers of bladder cancer: A pre- and post-operative evaluation," J. Pharm. Biomed. Anal. **124**, 22–25 (2016).
5. B. R. Davies, M. O'Donnell, G. C. Durkan, P. S. Rudland, R. Barraclough, D. E. Neal, and J. K. Mellon, "Expression of S100A4 protein is associated with metastasis and reduced survival in human bladder cancer," J. Pathol. **196**(3), 292–299 (2002).
6. Y. Sagara, Y. Miyata, T. Iwata, S. Kanda, T. Hayashi, H. Sakai, and H. Kanetake, "Clinical significance and prognostic value of S100A4 and matrix metalloproteinase-14 in patients with organ-confined bladder cancer," Exp. Ther. Med. **1**(1), 27–31 (2010).
7. F. Fei, J. Qu, M. Zhang, Y. Li, and S. Zhang, "S100A4 in cancer progression and metastasis: A systematic review," Oncotarget **8**(42), 73219–73239 (2017).
8. J. L. Turnier, N. Fall, S. Thornton, D. Witte, M. R. Bennett, S. Appenzeller, M. S. Klein-Gitelman, A. A. Grom, and H. I. Brunner, "Urine S100 proteins as potential biomarkers of lupus nephritis activity," Arthritis Res. Ther. **19**(1), 242 (2017).
9. S. F. Shariat, J. A. Karam, Y. Lotan, and P. I. Karakiewizc, "Critical evaluation of urinary markers for bladder cancer detection and monitoring," Rev. Urol. **10**(2), 120–135 (2008).
10. M. Viola-Magni, S. Cataldi, and D. Marocco, "Bladder cancer markers and recent innovations," in *Bladder Cancer - Management of NMI and Muscle-Invasive Cancer* (IntechOpen, 2017), pp. 63–94.
11. E. Luan, H. Shoman, D. M. Ratner, K. C. Cheung, and L. Chrostowski, "Silicon photonic biosensors using label-free detection," Sensors (Basel) **18**(10), E3519 (2018).
12. W. Pongruengkiat and S. Pechprasarn, "Whispering-gallery mode resonators for detecting cancer," Sensors (Basel) **17**(9), 2095 (2017).
13. E. Kim, M. D. Baaske, and F. Vollmer, "Towards next-generation label-free biosensors: recent advances in whispering gallery mode sensors," Lab Chip **17**(7), 1190–1205 (2017).
14. Y. Sun and X. Fan, "Optical ring resonators for biochemical and chemical sensing," Anal. Bioanal. Chem. **399**(1), 205–211 (2011).
15. J. T. Kindt and R. C. Bailey, "Biomolecular analysis with microring resonators: applications in multiplexed diagnostics and interaction screening," Curr. Opin. Chem. Biol. **17**(5), 818–826 (2013).
16. M. Iqbal, M. A. Gleeson, B. Spaugh, F. Tybor, W. G. Gunn, M. Hochberg, T. Baehr-jones, R. C. Bailey, L. C. Gunn, R. Resonators, H. Optical, M. Iqbal, M. A. Gleeson, B. Spaugh, F. Tybor, W. G. Gunn, M. Hochberg, T. Baehr-jones, R. C. Bailey, and L. C. Gunn, "Label-Free biosensor arrays based on silicon scanning instrumentation," IEEE J. Sel. Top. Quantum Electron. **16**(3), 654–661 (2010).
17. L. Gounaridis, P. Groumas, E. Schreuder, G. Tsekenis, A. Marousis, R. Heideman, H. Avramopoulos, and C. Kouloumentas, "High performance refractive index sensor based on low Q-factor ring resonators and FFT processing of wavelength scanning data," Opt. Express **25**(7), 7483–7495 (2017).
18. I. M. White and X. Fan, "On the performance quantification of resonant refractive index sensors," Opt. Express **16**(2), 1020–1028 (2008).
19. W. Bogaerts, P. De Heyn, T. Van Vaerenbergh, K. De Vos, S. Kumar Selvaraja, T. Claes, P. Dumon, P. Bienstman, D. Van Thourhout, and R. Baets, "Silicon microring resonators," Laser Photonics Rev. **6**(1), 47–73 (2012).
20. A. L. Washburn, M. S. Luchansky, A. L. Bowman, and R. C. Bailey, "Quantitative, label-free detection of five protein biomarkers using multiplexed arrays of silicon photonic microring resonators," Anal. Chem. **82**(1), 69–72 (2009).

21. M. K. Park, J. S. Kee, J. Y. Quah, V. Netto, J. Song, Q. Fang, E. M. La Fosse, and G. Q. Lo, "Label-free aptamer sensor based on silicon microring resonators," Sens. Actuators B Chem. **176**, 552–559 (2013).

22. A. Samusenko, R. Guider, L. Pavesi, G. Pucker, T. Chalyan, D. Gandolfi, and M. Ghulinyan, "A SiON Microring Resonator-Based Platform for Biosensing at 850 nm," J. Lit. Technol. **34**(3), 969–977 (2016).

23. G. Besselink, R. Heideman, E. Schreuder, L. Wevers, F. Falke, and H. Van den Vlekkert, "Performance of arrayed microring resonator sensors with the TriPleX platform," J. Biosens. Bioelectron. **7**(2), 1000209 (2016).

24. A. L. Washburn, W. W. Shia, K. A. Lenkeit, S.-H. Lee, and R. C. Bailey, "Multiplexed cancer biomarker detection using chip-integrated silicon photonic sensor arrays," Analyst (Lond.) **141**(18), 5358–5365 (2016).

25. S. Schmidt, J. Flueckiger, W. Wu, S. M. Grist, S. Talebi Fard, V. Donzella, P. Khumwan, E. R. Thompson, Q. Wang, P. Kulik, X. Wang, A. Sherwali, J. Kirk, K. C. Cheung, L. Chrostowski, and D. Ratner, "Improving the performance of silicon photonic rings, disks, and Bragg gratings for use in label-free biosensing," Proc. SPIE **9166**, 91660M (2014).

26. J. T. Kirk, N. D. Brault, T. Baehr-Jones, M. Hochberg, S. Jiang, and D. M. Ratner, "Zwitterionic polymer-modified silicon microring resonators for label-free biosensing in undiluted human plasma," Biosens. Bioelectron. **42**(1), 100–105 (2013).

27. A. L. Washburn, L. C. Gunn, and R. C. Bailey, "Label-free quantitation of a cancer biomarker in complex media using silicon photonic microring resonators," Anal. Chem. **81**(22), 9499–9506 (2009).

28. Y. Shin, A. P. Perera, and M. K. Park, "Label-free DNA sensor for detection of bladder cancer biomarkers in urine," Sens. Actuators B Chem. **178**, 200–206 (2013).

29. J. D. B. Bradley, F. Ay, K. Wörhoff, and M. Pollnau, "Fabrication of low-loss channel waveguides in Al_2O_3 and Y_2O_3 layers by inductively coupled plasma reactive ion etching," Appl. Phys. B **89**, 311–318 (2007).

30. G. Este, "Reactive deposition of low loss Al_2O_3 optical waveguides by modified dc planar magnetron sputtering," J. Vac. Sci. Technol., A **2**(3), 1238–1247 (1984).

31. G. N. van den Hoven, R. J. I. M. Koper, A. Polman, C. van Dam, J. W. M. van Uffelen, and M. K. Smit, "Net optical gain at 1.53 μm in Er-doped Al_2O_3 waveguides on silicon," Appl. Phys. Lett. **68**(14), 1886–1888 (1996).

32. E. H. Bernhardi, H. A. G. M. van Wolferen, L. Agazzi, M. R. H. Khan, C. G. H. Roeloffzen, K. Wörhoff, M. Pollnau, and R. M. de Ridder, "Ultra-narrow-linewidth, single-frequency distributed feedback waveguide laser in Al_2O_3:Er^{3+} on silicon," Opt. Lett. **35**(14), 2394–2396 (2010).

33. J. D. Bradley, R. Stoffer, L. Agazzi, F. Ay, K. Wörhoff, and M. Pollnau, "Integrated Al_2O_3:Er^{3+} ring lasers on silicon with wide wavelength selectivity," Opt. Lett. **35**(1), 73–75 (2010).

34. N. Li, E. S. Magden, Z. Su, N. Singh, A. Ruocco, M. Xin, M. Byrd, P. T. Callahan, J. D. B. Bradley, C. Baiocco, D. Vermeulen, and M. R. Watts, "Broadband 2-μm emission on silicon chips: monolithically integrated Holmium lasers," Opt. Express **26**(3), 2220–2230 (2018).

35. T. Reynolds, N. Riesen, A. Meldrum, X. Fan, J. M. M. Hall, T. M. Monro, and A. François, "Fluorescent and lasing whispering gallery mode microresonators for sensing applications," Laser Photonics Rev. **11**, 1600265 (2017).

36. L. He, Ş. K. Özdemir, J. Zhu, W. Kim, and L. Yang, "Detecting single viruses and nanoparticles using whispering gallery microlasers," Nat. Nanotechnol. **6**(7), 428–432 (2011).

37. E. H. Bernhardi, K. O. van der Werf, A. J. F. Hollink, K. Wörhoff, R. M. de Ridder, V. Subramaniam, and M. Pollnau, "Intra-laser-cavity microparticle sensing with a dual-wavelength distributed-feedback laser," Laser Photonics Rev. **7**(4), 589–598 (2013).

38. M. De Goede, L. Chang, M. Dijkstra, R. Obregon, J. Ramon-Azcon, E. Martinez, L. Padilla, J. Adan, F. Mitjans, and S. M. Garcia-Blanco, "Al_2O_3 Microresonator Based Passive and Active Biosensors," Int. Conf. Transparent Opt. Networks **2018**–**July**, 1–4 (2018).

39. Z. Su, N. Li, H. C. Frankis, E. S. Magden, T. N. Adam, G. Leake, D. Coolbaugh, J. D. B. Bradley, and M. R. Watts, "High-Q-factor Al_2O_3 micro-trench cavities integrated with silicon nitride waveguides on silicon," Opt. Express **26**(9), 11161–11170 (2018).

40. M. de Goede, M. Dijkstra, R. O. Núñez, E. Martínez, and S. M. García-Blanco, "High quality factor Al_2O_3 microring resonators for on-chip sensing applications," Proc. SPIE **10535**, 1053504 (2018).

41. S. K. Mishra, H. R. Siddique, and M. Saleem, "S100A4 calcium-binding protein is key player in tumor progression and metastasis: preclinical and clinical evidence," Cancer Metastasis Rev. **31**(1-2), 163–172 (2012).

42. S. C. Garrett, K. M. Varney, D. J. Weber, and A. R. Bresnick, "S100A4, a mediator of metastasis," J. Biol. Chem. **281**(2), 677–680 (2006).

43. L. Chrostowski, S. Grist, J. Flueckiger, W. Shi, X. Wang, E. Ouellet, H. Yun, M. Webb, B. Nie, Z. Liang, K. C. Cheung, S. A. Schmidt, D. M. Ratner, and N. A. F. Jaeger, "Silicon photonic resonator sensors and devices," Proc. SPIE **8236**, 823620 (2012).

44. J. Scheuer, "White light cavity formation and superluminal lasing near exceptional points," Opt. Express **26**(24), 32091–32102 (2018).

45. S. T. Fard, V. Donzella, S. A. Schmidt, J. Flueckiger, S. M. Grist, P. Talebi Fard, Y. Wu, R. J. Bojko, E. Kwok, N. A. F. Jaeger, D. M. Ratner, and L. Chrostowski, "Performance of ultra-thin SOI-based resonators for sensing applications," Opt. Express **22**(12), 14166–14179 (2014).

46. W. R. McKinnon, D. X. Xu, C. Storey, E. Post, A. Densmore, A. Delâge, P. Waldron, J. H. Schmid, and S. Janz, "Extracting coupling and loss coefficients from a ring resonator," Opt. Express **17**(21), 18971–18982 (2009).

47. X. Quan and E. S. Fry, "Empirical equation for the index of refraction of seawater," Appl. Opt. **34**(18), 3477–3480 (1995).

48. L. Padilla, S. Dakhel, and J. L. Hernández, "S100 to receptor for advanced glycation end-products binding assay: looking for inhibitors," Biochem. Biophys. Res. Commun. **446**(1), 404–409 (2014).
49. J. Hu, X. Sun, A. Agarwal, and L. C. Kimerling, "Design guidelines for optical resonator biochemical sensors," J. Opt. Soc. Am. B **26**(5), 1032–1041 (2009).